AGU PUBLICATIONS

JGR

Journal of Geophysical Research: Space Physics

RESEARCH ARTICLE

10.1002/2015JA021206

Key Points:

- Storm phases showed latitudinal and then longitudinal variations
- Nighttime positive and negative storms occurred at once over North America
- Maximum (minimum) solar radiation leads to positive (negative) storms in the polar caps

Correspondence to:
I. Horvath,
ihorvath@itee.uq.edu.au

Citation:
Horvath, I., and B. C. Lovell (2015), Positive and negative ionospheric storms occurring during the 15 May 2005 geomagnetic superstorm, *J. Geophys. Res. Space Physics*, *120*, 7822–7837, doi:10.1002/2015JA021206.

Received 11 MAR 2015
Accepted 5 AUG 2015
Accepted article online 10 AUG 2015
Published online 4 SEP 2015

Positive and negative ionospheric storms occurring during the 15 May 2005 geomagnetic superstorm

Ildiko Horvath[1] and Brian C. Lovell[1]

[1]Security and Surveillance Research Group, School of Information Technology and Electrical Engineering, University of Queensland, Brisbane, Queensland, Australia

Abstract This study focuses on the 15 May 2005 geomagnetic superstorm and aims to investigate the global variation of positive and negative storm phases and their development. Observations are provided by a series of global total electron content maps and multi-instrument line plots. Coupled Thermosphere-Ionosphere-Plasmasphere electrodynamics (CTIPe) simulations are also employed. Results reveal some sunward streaming plumes of storm-enhanced density (SED) over Asia and a well-developed midlatitude trough over North America forming isolated positive and negative storms, respectively. The simultaneous development of positive and negative storms over North America is also shown. Then, some enhanced auroral ionizations maintained by strong equatorward neutral winds appeared in the depleted nighttime ionosphere. Meanwhile, the northern nighttime polar region became significantly depleted as the SED plume plasma could not progress further than the dayside cusp. Oppositely, a polar tongue of ionization (TOI) developed in the daytime southern polar region. According to CTIP simulations, solar heating locally maximized (minimized) over the southern (northern) magnetic pole. Furthermore, strong upward surges of molecular-rich air created O/N_2 decreases both in the auroral zone and in the trough region, while some SED-related downward surges produced O/N_2 increases. From these results we conclude for the time period studied that (1) composition changes contributed to the formation of positive and negative storms, (2) strengthening polar convection and increasing solar heating of the polar cap supported polar TOI development, and (3) a weaker polar convection and minimized solar heating of the polar cap aided the depletion of polar plasma.

1. Introduction

How the coupled thermosphere-ionosphere system responds to solar activity is an important subject of space weather studies. While these studies cover a wide range of topics, the ionospheric response to geomagnetic storms is particularly significant to system researchers and model developers due to (1) the highly variable ionospheric response-time ranging from an hour to a few days; (2) the significant enhancement or depletion of ionospheric plasma, by up to a factor of 3, at low, middle, or high latitudes; and (3) the generation or suppression of ionospheric irregularities [*Sahai et al*., 2009]. Due to the variability of ionospheric *F* region responses and their drivers, storm studies focus on the development of ionospheric storms and their underlying mechanisms. If the plasma density increases (decreases) relative to the quiet time level due to the underlying storm dynamics, a positive (negative) ionospheric storm or phase is produced [*Danilov and Morozova*, 1985; *Schunk and Sojka*, 1996]. While negative ionospheric storms can cause serious blackouts both in high-frequency (HF) radio communications and in transionospheric Global Navigation Satellite Systems-based timing and positioning, positive ionospheric storms can significantly delay and scintillate radio signals [*Basu et al*., 2010; *Kintner et al*., 2007; *van der Meeren et al*., 2014]. As reported by various investigations, positive and negative ionospheric storms have been observed during all geomagnetic storm phases [*Abdu*, 1997; *Mendillo*, 2006; *Wang et al*., 2010].

The major drivers of ionospheric storms include thermospheric neutral winds, composition changes, and electric (**E**) fields of different origins [*Sastri et al*., 2000]. As a geomagnetic storm develops and unfolds, the most significant underlying geophysical processes include the heating of high-latitude thermosphere by enhanced energy deposition into the auroral zone. Resultant Joule heating triggers equatorward wind surges and the generation of atmospheric gravity waves propagating as traveling atmospheric disturbances (TADs) [*Prölss and Jung*, 1978] and traveling ionospheric disturbances (TIDs) [*Millward et al*., 1993]. TIDs move the ionospheric plasma and cause significant changes in thermospheric composition [*Roble et al*., 1982]. Meanwhile, **E** field of magnetospheric origin promptly penetrates (PPEF) from the polar region to the equator

[*Kikuchi et al*., 1978, 2008], subauroral polarization stream (SAPS) **E** field intensifies [*Foster and Burke*, 2002], and disturbance dynamo **E** field (DDEF) develops [*Blanc and Richmond*, 1980].

Recent superstorm studies focus on explaining the most significant ionospheric response driver effects in creating ionospheric storms via electrodynamic, dynamic, and chemical processes. The electrodynamic role of eastward PPEF both in enhancing the forward plasma fountain via the equatorial vertical upward $\mathbf{E} \times \mathbf{B}$ drift and in intensifying the development of equatorial ionization anomaly (EIA) is well understood [*Kelley et al*., 2004; *Tsurutani et al*., 2004; *Mannucci et al*., 2005]. During the process of forward fountain circulation [*Balan and Bailey*, 1995], negative storms at equatorial latitudes (i.e., where the EIA trough region occurs) and positive storms with the aid of mechanical wind effects [*Balan et al*., 2010, 2013; *Lu et al*., 2012] at low latitudes (i.e., where the EIA crests develop) are created. Meanwhile, equatorward (poleward) directed thermospheric neutral winds and TADs propagating equatorward from auroral latitudes can also lead to the development of positive (negative) storms via dynamic processes such as moving the ionization to higher (lower) altitudes where the recombination rates are lower (higher) [*Balan et al*., 2010]. At subauroral and polar latitudes, positives storms are produced by the development of storm-enhanced density (SED) [*Foster*, 1993] and by the source SED plume plasma (i.e., low-altitude signature of plasmaspheric tail [*Su et al*., 2001]) propagating into the polar region through the dayside cusp and thus forming a polar tongue of ionization (TOI) [*Foster et al*., 2005], respectively. The equatorward expansion of polar two-cell convection and plasma transfer from lower latitudes, the latter is due to the so-called "snow-plow" effects [*Foster*, 1993], are the major causative mechanisms. Meanwhile, high-latitude heat deposition and SED-related SAPS **E** field effects enhance the local plasma temperatures at auroral latitudes via Joule heating and in the SAPS channel via frictional heating, respectively. As the midlatitude trough develops in the SAPS channel, the resultant SAPS-related upward plasma surges deepen the midlatitude trough and thus contribute to the development of negative storms at trough latitudes. Meanwhile, away from the SAPS channel, some convergent downward plasma surges dominate [*Wang et al*., 2012]. These upward and downward plasma surges create also composition changes by decreasing the ratio of O and N_2 (indicated as O/N_2) in the auroral and trough regions and by increasing O/N_2 away from them, respectively [*Cander and Mihajlovic*, 2005; *Wang et al*., 2012]. TAD-related downward surges can also turn positive storms into negative storms [*Vijaya Lekshmi et al*., 2007].

As the number of receiver sites of the Global Positioning System (GPS) has been dramatically increased in the last two decades and thus provides sufficient and accurate data for monitoring the global total electron content (TEC) reliably, TEC line plots constructed with data from individual receiver sites and global TEC maps have been equally utilized for studying ionospheric storms locally and globally [*Scharroo and Smith*, 2010]. More recently, *Galav et al*. [2014] detected midlatitude daytime (nighttime) TEC increases (decreases) occurring simultaneously over the Northern Hemisphere during the main phase of the 15 May 2005 geomagnetic superstorm. While the TEC time series constructed for Poligan (POL2; 33.72°N, geomagnetic) tracked daytime increases that were due to both storm time PPEF and storm-induced equatorward neutral winds, the TEC time series constructed for Algonquin (ALGO; 55.93°N) detected depletions that were attributed to the midlatitude trough [*Galav et al*., 2014]. Some earlier studies covering this geomagnetic superstorm focused on the low-latitude regions of the Indian zone [*Dashora et al*., 2009] and Southeast Asia [*Sharma et al*., 2011]. Although the findings of all these studies are significant and are potentially useful to system engineers and ionospheric model developers, the observational results are from specific locations. Thus, the global perspective regarding the variation of positive and negative ionospheric storms during this geomagnetic superstorm is still unclear and thus warrants further investigations. Hence, we aim in this study to investigate the development of positive and negative ionospheric storms on a global scale by utilizing a series of global GPS TEC maps that are coupled with multi-instrument observations and model simulations. These maps reveal the increasingly better development of a positive (negative) phase at low and middle latitudes in the 0–180°E (180–360°E) sector during the local daytime (nighttime) hours of the initial and main phases and its maximizing early in the recovery phase. An interesting scenario depicts some simultaneously appearing positive and negative storms over North America during the local nighttime hours. For the first time, this study demonstrates that the northern polar region on the nightside favored the development of strong plasma depletions, while a distinct polar TOI appeared in the southern polar region on the dayside.

2. Database and Methodology

We have constructed a complex database containing multi-instrument ground- and space-based data and various model simulations that are all available in the public domain. This database covers the magnetically

Table 1. List of Ground-Based Stations Providing Data for This Study

Station Name	Geographic Latitude (°N)	Geographic Longitude (°E)	Geomagnetic Latitude (°N)
Alibag (ABG)	18.64	72.87	10.19
Chilton (RL052)	51.60	358.70	49.90
Goosebay (GSJ53)	53.30	299.60	61.18
Jicamarca (JIC)	−11.92	281.03	−1.55
King Salmon (KS759)	58.40	203.60	63.50
Mundaring (MU43K)	−32.00	116.40	−43.20
Piura (PIU)	−5.01	278.93	5.11
Port Stanley (PSJ5J)	−51.70	302.20	−41.69
Puerto Rico (PRJ18)	18.50	292.80	18.26
Rostov (RV149)	47.20	39.70	42.40
Tashkent (TQ241)	41.30	69.60	32.50
Thule (THL)	77.48	290.83	87.68
Townsville (TV51R)	−19.70	146.90	−28.40
Trivandrum (TVM)	8.55	76.90	0.29
Wallops Is (WP937)	37.80	284.50	49.20

quiet day of 14 ($\sum Kp = 12+$) and disturbed day of 15 ($\sum Kp = 45+$) May 2005. We have prepared global and polar GPS TEC maps by utilizing ground-based vertical TEC values (total electron content unit (TECU), 1 TECU = 10^{16} el/m^2) offered by Massachusetts Institute of Technology's Madrigal Database and Jet Propulsion Laboratory's (JPL) Global Ionosphere Map (GIM) program employing data from 402 ground-based GPS stations (ftp://cddis.gsfc.nasa.gov/gnss/reports/daily/cddis_summary.2005). These GPS TEC maps are complemented by space-based multi-instrument in situ measurements of the Defense Meteorological Satellite Program (DMSP) taken at ~840 km altitude. As part of our methodology, we have constructed manually and analyzed latitudinal profiles of ion density (Ni; i^+/cm^3), electron temperature (T_e; K), cross-track plasma drifts (V_Y, V_Z; m/s) in the east-west (Y) or zonal and north-south (Z) or vertical directions, and cross-track plasma flows (F_Z; i^+/(cm^3 s)) [*Horvath*, 2007]. Ground-based ionosonde data plus magnetometer data from some selected stations (see Table 1) permitted monitoring F_2 layer height (h_mF_2; km) and electron density via the parameter of critical frequency (f_oF_2; MHz) plus magnetic field variations, respectively. Auroral electron energy flux (ergs/s/cm^2) images are from the Global Ultraviolet Imager (GUVI), which is one of the four scientific instruments aboard the NASA Thermosphere-Ionosphere-Mesosphere Energetics and Dynamics satellite [*Christensen et al.*, 2003]. Although GUVI provides O/N_2 measurements, the areas of interest were not covered and we have utilized simulated values. Provided by the Community Coordinated Modeling Center (CCMC), model simulations are from the Coupled Thermosphere-Ionosphere-Plasmasphere (CTIP) and CTIP electrodynamics (CTIPe) [*Fuller-Rowell et al.*, 2002]. We have utilized model simulations for investigating the spatial variation of some important variables such as O/N_2 plus solar heating (P_{solar}; W/kg) and Joule heating (P_{Joule}; W/kg). Polar convection maps, inferred from Super Dual Auroral Radar Network HF measurements, were obtained from Virginia Tech via interactive plotting. Geomagnetic activity indices employed include the 1 min time resolution *SYM-H* (nT), *ASY-H* (nT), and *AE* (nT) data. Meanwhile, the polar cap north (PCN; mV/m) index from Thule (see Table 1) allowed us to compute the values of cross Polar Cap Potential (PCP) drop as Φ_{PC} (kV) = 19.35PCN + 8.78 [*Troshichev et al.*, 1996]. Interplanetary magnetic field (IMF) measurements are from the Advance Composition Explorer (ACE) satellite. In order to compare IMF and geomagnetic values, the ACE data were delayed with ~33 min according to the satellite position at ~(249.16; 8.75; −12.56) R_E in GSE coordinates. All the raw and reduced data and the various model simulations utilized for this study are preserved and added to our data storage.

3. Results and Interpretations

3.1. Interplanetary and Geomagnetic Conditions

The 15 May 2005 geomagnetic superstorm was the most intense geomagnetic storm of year 2005. Its solar, interplanetary and geophysical conditions have been investigated by various studies [e.g., *Bisi et al.*, 2010, and references therein]. Some characteristic variables such as the IMF $\mathbf{B_Z}$ component, various geomagnetic

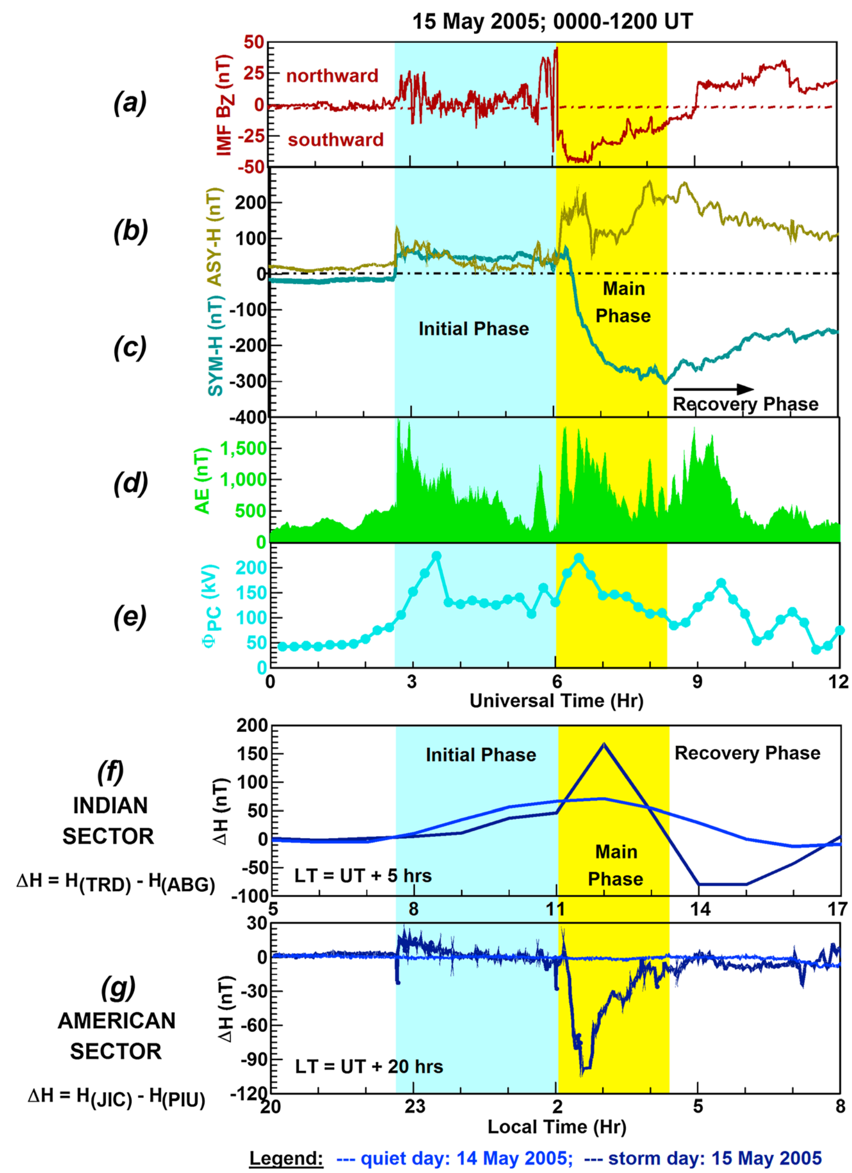

Figure 1. (a–e) The line plots depict a small collection of geophysical variables characterizing the 15 May 2005 superstorm during which a series of substorms occurred. Some e-EEJ and w-EEJ events also took place in the (f) Indian and (g) American longitude sectors.

indices and the modeled Φ_{PC} are shown in Figure 1 where the shaded areas mark the initial and main phases. While the *SYM-H* and *ASY-H* indices depict the severity of this geomagnetic storm, the *AE* index allowed us to infer auroral activity and high-latitude energy deposition events. Furthermore, the variation of modeled cross PCP drop (Φ_{PC}) implies the variation of magnetospheric convection and provides also a proxy for an **E** field of magnetospheric origin.

At 0240 UT, the onset of a long-lasting initial phase (0240–0600 UT) is clearly indicated by the simultaneous and sudden increases of *SYM-H*, *ASY-H*, and *AE* (to ~2000 nT) and by the gradual but large increase of Φ_{PC} (from 100 to 230 kV). At ~0600 UT, the main phase began with the southward turning of $\mathbf{B_Z}$, when the *AE* (to ~1800 nT) and *ASY-H* indices along with Φ_{PC} (from 120 to 220 kV) increased simultaneously. The suddenly decreasing *SYM-H* index reached −305 nT at ~0820 UT registering a superstorm and the onset of the recovery phase. Soon after that, at ~0900 UT, $\mathbf{B_Z}$ turned northward and *AE* increased (to ~1600 nT) for the third time. These three *AE* increases imply a series of three substorms, one during each geomagnetic storm phase.

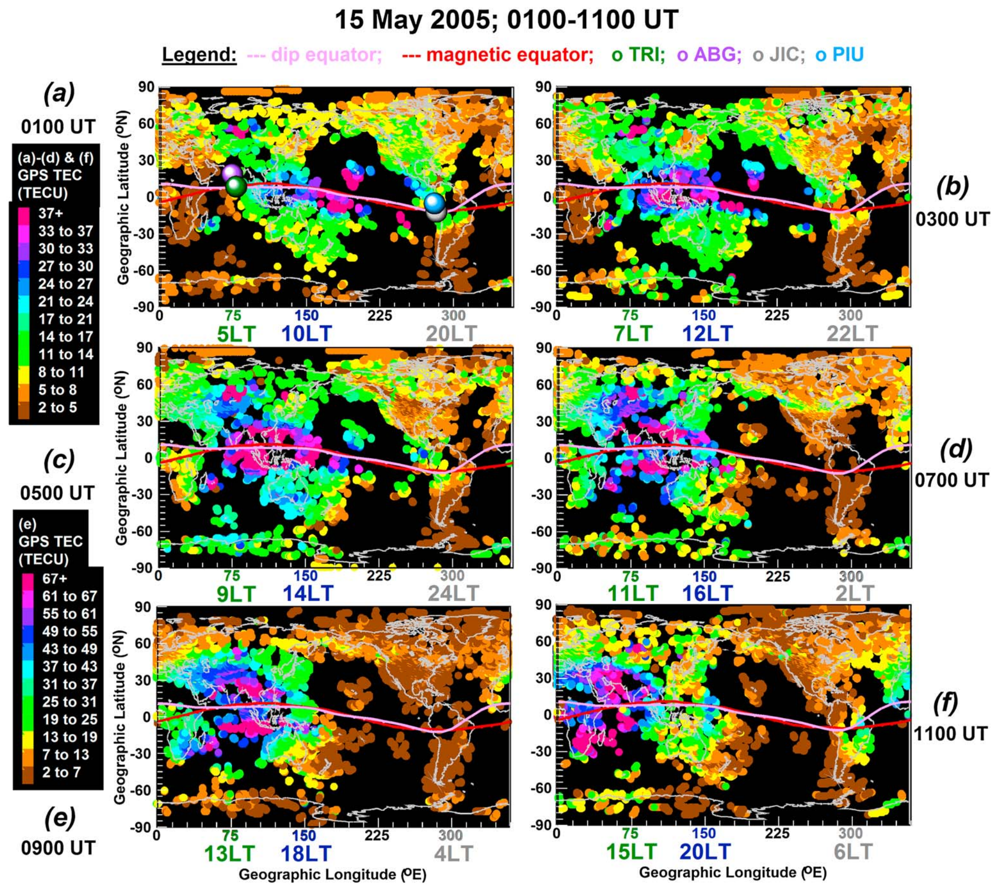

Figure 2. (a–f) A series of GPS TEC maps, where each maps is constructed with 20 min worth of data, depicts in 2 h intervals the ionosphere's response to this superstorm. In each map, LT values are indicated for 75°E, 150°E, and 300°E geographic longitudes. In Figure 2a, the first map illustrates also the locations of magnetometer stations utilized for this study.

Regarding the initial phase-related substorm, *Kozyreva and Kleimenova* [2007] specified this event as a "polar cap substorm" triggered by hydromagnetic waves that directly penetrated from the solar wind into the auroral region and from there to the polar cap. These hydromagnetic waves were the drivers of the disturbance **E** field, which penetrated from the polar cap to the equator and of which signature can be seen both in the polar cap region as the first Φ_{PC} intensification and at the equator as indicated by the magnetometer observations (see details below).

In order to get an indication how the equatorial vertical **E** × **B** drift varied in time and longitude under these disturbed conditions, we have computed ΔH (nT) values as $H_{(equ)} - H_{(non\text{-}equ)}$ [*Anderson et al.*, 2002] for quiet and storm days and for the daytime (~75°E; geographic) and nighttime (~280°E) sectors (see Figures 1f and 1g). While the quiet time ΔH plots illustrate ionospheric equatorial electrojet (EEJ) current and therefore ionospheric zonal (east-west) **E** field variations, the storm time ΔH plots depict variations due to the net perturbation **E** field (i.e., PPEF and/or DDEF additionally to the ionospheric zonal **E** field). During the initial phase, a weak westward EEJ (abbreviated as w-EEJ) developed in the Indian daytime sector while a weak eastward EEJ (abbreviated as e-EEJ) occurred in the American nighttime sector. The causative weak perturbation **E** field was possibly generated by the polar cap substorm and was communicated with a westward (eastward) polarity in the daytime (nighttime) sector during the initial phase. An opposite scenario occurred during the main phase when an e-EEJ (w-EEJ) developed in the Indian daytime (American nighttime) sector. Their underlying perturbation **E** field was possibly an undershielding **E** field with an eastward (westward) polarity in the daytime (nighttime) sector. This is suggested by the rapid increase of Φ_{PC} (from 130 to 220 kV) and southward turning of $\mathbf{B_Z}$ (to −50 nT) during 0600–0700 UT implying the rapid increase of magnetospheric convection and the temporary equatorward movement of the shielding layer [e.g., *Fejer et al.*, 2007]. During the recovery

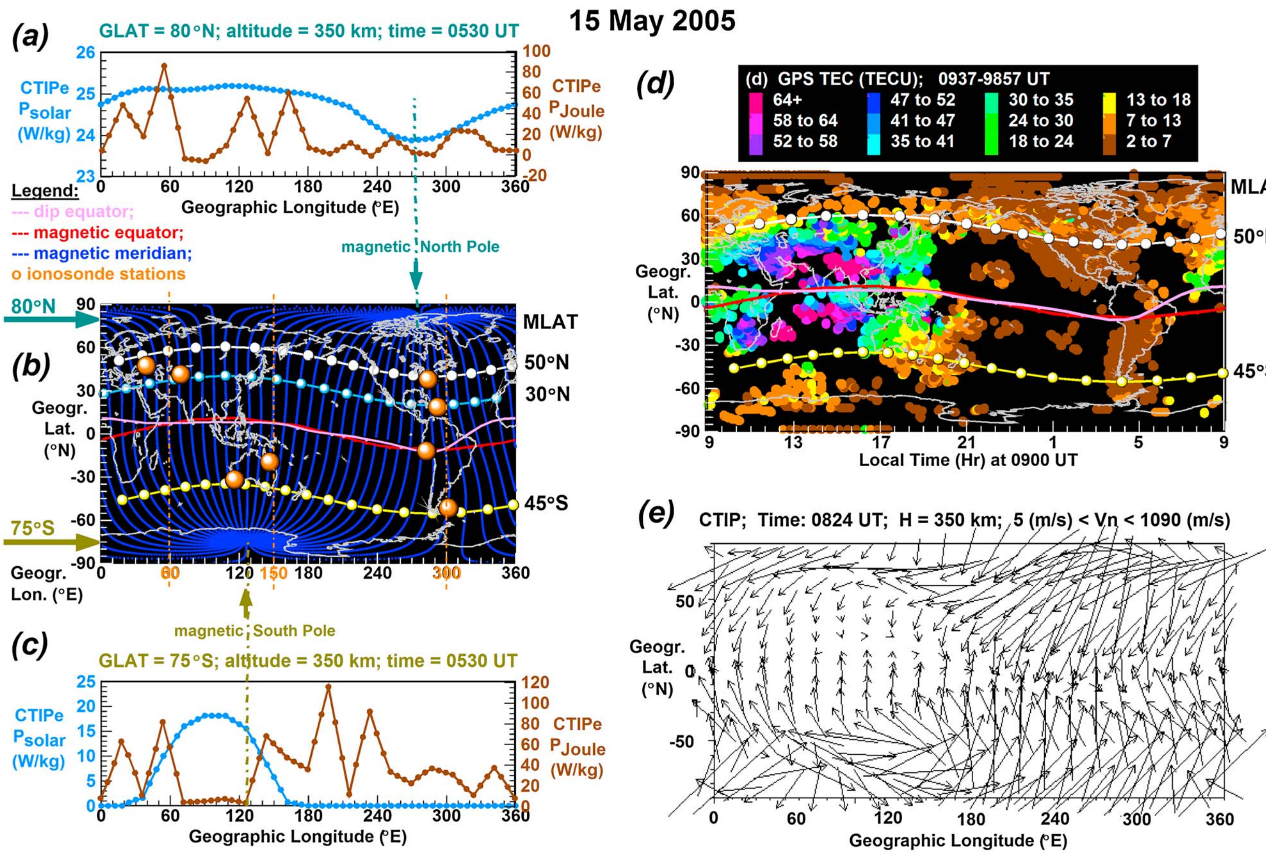

Figure 3. The (b) global map of magnetic meridians depicts the locations of ionosonde stations employed and some geomagnetic latitudes (50°N, 30°N, and 45°S) aiding our analysis. For the (a) northern and (c) southern magnetic poles, the CTIPe simulated P_{solar} and P_{Joule} line plots illustrate the longitudinal variation of solar heating and Joule heating, respectively. (d) The global GPS TEC map depicts a strong positive phase over the daytime hemisphere and a substantial negative phase over the nighttime hemisphere. (e) CTIP-generated wind vector map shows strong equatorward neutral winds in the geomagnetic latitude region of 50°N–45°S maximizing on the nightside.

phase, the EEJ was very weak in the nighttime American sector but a strong w-EEJ developed in the daytime Indian sector possibly due to the domination of the combined effects of westward DDEF and westward overshielding PPEF. The latter is suggested by the decrease of Φ_{PC} (to 80 kV) implying the decrease of magnetospheric convection and the temporary poleward movement of the shielding layer and by the northward turning of $\mathbf{B_Z}$ (from −10 to 20 nT) [e.g., *Fejer et al.*, 2007].

3.2. Global GPS TEC Observations

How the ionosphere responded to these **E** field variations is illustrated in Figure 2 with a set of six global GPS TEC maps covering the time period of 0100–1100 UT in 2 h time intervals. Each map was constructed with ~20 min worth of data in order to maintain good data coverage. Aiding our analysis, two sets of TEC color scales are utilized, the geomagnetic and dip equators are also plotted, and the local time values are indicated for the Indian (75°E), Australian (150°E), and American (300°E) longitude sectors. These maps depict the development of some large-scale ionospheric features such as the EIA, SED, and auroral and polar cap enhancements creating positive phases and the midlatitude trough creating a negative phase. There is a time delay of ~1–2 h between the underlying **E** field events indicated by the above described time series and the development of resultant ionospheric features tracked by the TEC maps. This is usual during disturbed time periods [*Dashora et al.*, 2009].

Figure 2a illustrates the quiet time ionospheric conditions prior to the initial phase during which the EIA was well developed over the mid-Pacific. Covering the initial phase, Figures 2b and 2c tracked the building up of the EIA (>37 and 33–37 TECU; indicated in red and pink, respectively) over the daytime region (0–180°E).

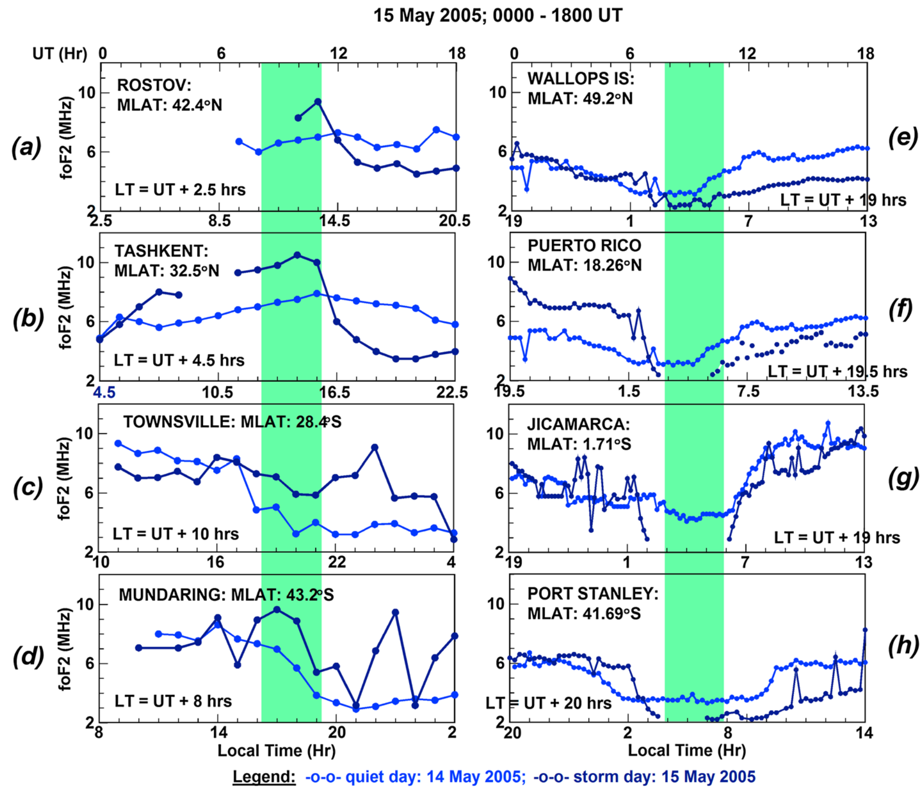

Figure 4. A series of f_oF_2 line plots illustrates that the most intensive (a–d) positive and (e–h) negative storm phases formed during 0800–1100 UT. These positive and negative storm phases shown in Figures 4a–4d are over the daytime Asian-Australian region and illustrated in Figures 4e–4h are in the nighttime America sector, respectively. The shaded interval in green indicates the main phase/recovery phase interface.

Due to the small eastward perturbation **E** field in the American nighttime sector, the EIA appeared in a less developed form (17–21 TECU; indicated in green) compared to its daytime counterpart. Also in the American sector, the TEC decreased to 2–5 TECU (indicated in dark brown) at midlatitudes and slightly increased to 8–11 TECU (indicated in yellow) in the northern polar region. In Figure 2c, the midlatitude trough (2–5 TECU; indicated in dark brown) is well visible and is situated equatorward of some auroral enhancements (8–11 TECU; indicated in yellow) over North America, while the sunward (westward) progressing SED plume plasma (24–27 TECU; indicated in blue) over Asia is apparent and possibly developed due to the polar cap substorm related perturbation **E** field. Early in the main phase (see Figure 2d), the features of SED plume (30–33 TECU; indicated in purple) and auroral enhancement (17–21 TECU; indicated in light green) became better developed possibly under the effects of undershielding PPEF. Later on during the main phase (see Figures 2d and 2e), when this undershielding PPEF became increasingly intensified, the EIA declined in the American sector under the domination of westward PPEF and the TEC decreased mostly to a minimum of 2–5 TECU (indicated in dark brown). Oppositely, the TEC had continued building up in the daytime 0–180°E region under the domination of eastward PPEF and reached maximum values at the EIA crests (>67 TECU; indicated in red). Early in the recovery phase (see Figure 2f), the TEC started decreasing (14–17 TECU; indicated in light green) in the Australian sector as the westward overshielding PPEF became active. Meanwhile, the TEC remained low in the American sector and over the Eastern Pacific (5–8 and 2–5 TECU; indicated in orange and dark brown).

3.3. Ionosonde Observations of Positive and Negative Storms

With Figure 3, we further demonstrate with ionosonde observations the major positive and negative storms occurring during the main phase and early in the recovery phase. In Figure 3b, the global map depicts the station locations, the modeled magnetic meridians, some geomagnetic latitudes (50°N, 30°N, and 45°S) aiding our analysis, and the magnetic and dip equators. Supporting our investigations, two sets of CTIPe

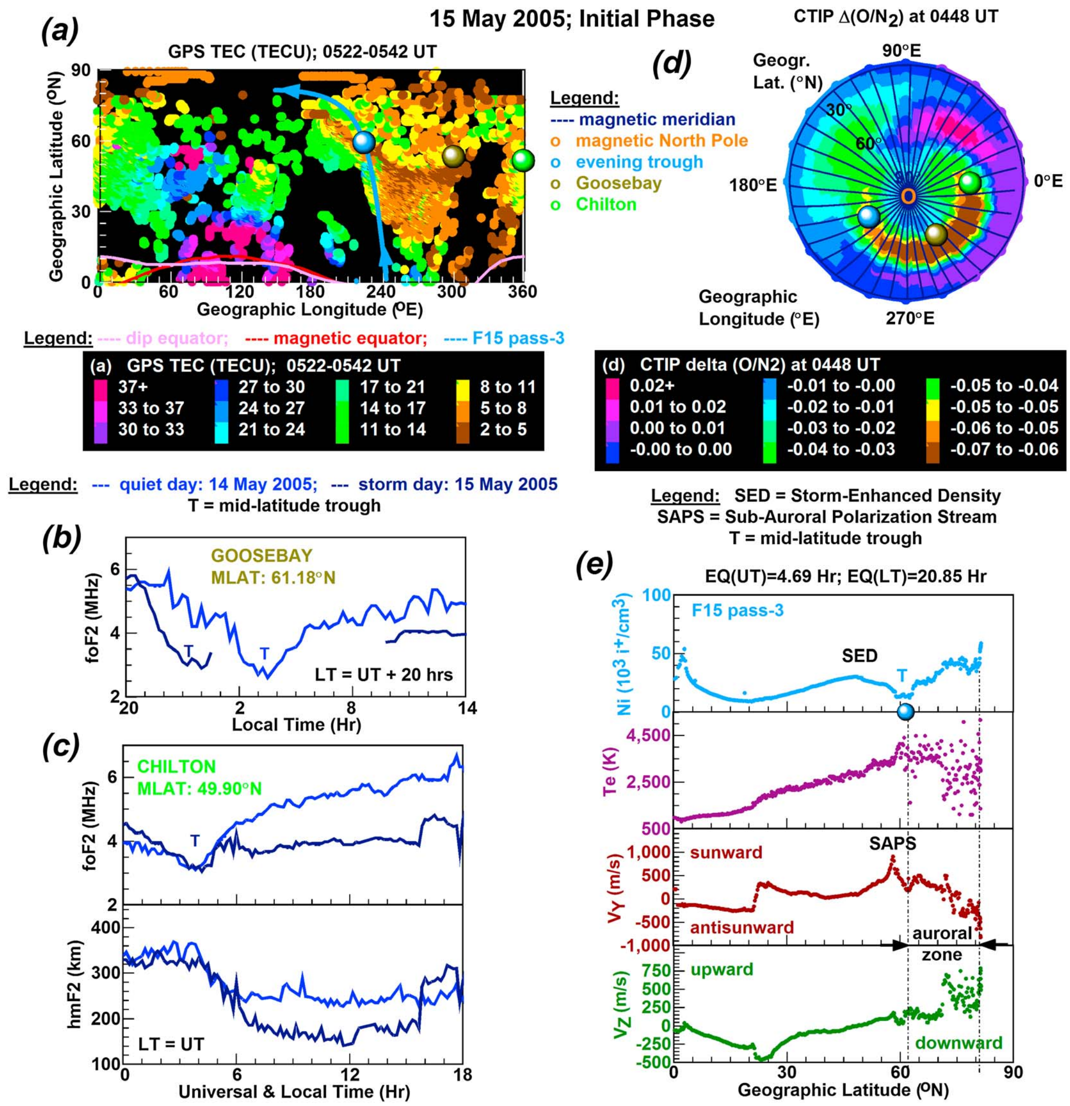

Figure 5. The (a) GPS TEC map and the (d) CTIP $\Delta(O/N_2)$ polar plot show the SED plume plasma and the midlatitude trough, plus their corresponding signatures appearing in thermospheric composition changes as increases and depletions, respectively. The (b) Goosebay f_oF_2 line plot depicts the midlatitude trough, while the F_2 layer height variations are also shown for (c) Chilton. (e) A set of multi-instrument DMSP line plots depict the trough and its surrounding plasma density features plus their underlying thermal characteristics and plasma drifts in the local evening sector.

simulated P_{solar} and P_{Joule} line plots (see Figures 3a and 3c, respectively) illustrate the longitudinal variation of solar heating and Joule heating, respectively, at the polar geographic latitudes of 80°N and 75°S, just before the end of the initial phase (0530 UT). At 0530 UT, the solar heating locally decreased in the vicinity of magnetic North Pole on the nightside but reached its local maximum near the magnetic South Pole on the dayside leaving the southern polar region highly solar heated. Meanwhile, the Joule heating locally decreased over each magnetic pole. Regarding the ionosonde stations employed (see Figure 3b), these are situated in the American sector at these designated magnetic latitudes and along similar magnetic meridians. In the 0–180°E region, the stations are close to the designated magnetic latitudes but are scattered over Australia and Asia. We exemplify here the beginning of the recovery phase with a GPS TEC map covering the period of 0937–0957 UT (see Figure 3d) and with a CTIP-generated wind vector map simulated for 0824 UT and 350 km altitude (see Figure 3e). By considering the 50°N–45°S magnetic latitude region, it is apparent that a large positive phase developed in the 0–180°E daytime sector with the mechanical aid of strong equatorward neutral winds. Meanwhile, minimum TECs (2–7 TECU; indicated in dark brown) created a large negative phase in the American nighttime sector where apparently the mechanical effects of the strongest equatorward directed neutral winds occurring at this time could not increase the ionization. From these observations we conclude a strong longitudinal-dependent variation of the ionospheric storm. In Figure 4 we further demonstrate these positive and negative phases with some f_oF_2 time series and with plotting quiet day and storm day data together. A 3 h (0800–1100 UT) time interval, covering largely the main phase/recovery phase interface, is marked by the shaded interval in light green. These f_oF_2 time series demonstrate the increase (decrease) of storm time electron density with respect to the quiet time conditions during the highlighted interval of 0800–1100 UT in the geomagnetic 50°N–45°S region of the Asian-Australian (American) sector. While the largest ~40% increase seen in the Tashkent (32.5°N) f_oF_2 data was due to the local SED features (see Figure 2e), the occurrence of largest ~58.5% decrease over Jicamarca (1.71°S; close to the dip equator) was caused by a strong westward directed net **E** field (see local ΔH line plots in Figure 1g) that was dominated by the undershielding westward PPEF.

3.4. Midlatitude Trough Over North America During the Initial Phase

Figure 5 illustrates the various characteristics of the midlatitude trough during the initial phase with a variety of data plots. These include a GPS TEC map constructed with data in Figure 2c, a polar map of CTIP $\Delta(O/N_2)$ where $\Delta(O/N_2)$ is computed as $O/N_{2(\text{storm time})}$-$O/N_{2(\text{quiet time})}$, and some line plots constructed with Goosebay and Chilton ionosonde data and with the multi-instrument DMSP data. To describe these observations, the GPS TEC map tracked during 0522–0542 UT a well-developed midlatitude trough (2–5 TECU; indicated in dark brown) and some auroral ionization on its poleward side (8–11 TECU; indicated in yellow) over a larger region of the North American sector while the SED plume plasma (24–27 TECU; indicated in blue) was progressing sunward or westward over Asia. According to this GPS TEC map, showing also the ionosonde station locations, the trough appeared also over Goosebay and Chilton and was detected first in the storm time f_oF_2 data at ~0300 UT (marked as "T" in dark blue) but latter detections over Goosebay were prevented by a data gap. As seen in the quiet time Goosebay data, the quiet time trough appeared at a later time (at ~0730 UT, marked as "T" in blue). Thus, the earlier occurrence of storm time trough over Goosebay decreased largely (~45% at 0300 UT) the quiet time electron densities. Over Chilton, the quiet time and storm time trough occurred during 0300–0500 T but the storm time electron densities remained depleted during 0700–1200 UT. During the trough occurrence, the F_2 layer height reached its local maximum (~360 km) due to the underlying frictional heating causing upward surges (see details below) and thus moving the F_2 layer to higher altitudes. But as the trough moved away from Chilton, the storm time F_2 layer height decreased from ~200 km (at 0700 UT) to ~140 km (at 1200 UT) compared to the nearly steady quiet time value of ~260 km. Both the depletion of electron density and the lowering of F_2 layer during 0700–1200 UT (0700–1200 LT) over Chilton indicates downward surges of oxygen-rich air caused by convergent wind flows occurring away from the trough [*Wang et al.*, 2012].

The polar $\Delta(O/N_2)$ plot constructed for 0448 UT, when the trough appeared, shows at 300 km altitude the storm-related thermospheric composition differences. Here the storm time trough location detected by DMSP and the data providing ionosonde stations are also plotted. Thus, this polar plot reveals that at trough latitudes there is a well-defined decrease in $\Delta(O/N_2)$ (ranging from -0.05 to -0.07; indicated in yellow, orange, and dark brown) that is due to the strong upward surges occurring in the trough region because of the intense frictional heating and thus transporting upward molecular-rich air from the lower thermosphere. These results are in good agreements with the Thermosphere Ionosphere Electrodynamics general circulation model (TIE-GCM) simulated results of *Wang et al.* [2012] obtained for a moderately active ($Kp = 4+$) period. Another interesting feature is the signature of SED plume plasma shown by the $\Delta(O/N_2)$ polar plot as a local maximum (>0.02 and 0.01–0.02; indicated in red and pink, respectively) on the equatorward side of the trough and over the European sector (0–30°E). In good agreement with the results of *Wang et al.* [2012], such $\Delta(O/N_2)$ increase is due to the downward surge of oxygen-rich air. Adding to their study, our results demonstrate that such surges can be associated with the downward flowing SED plume plasma.

In order to further demonstrate the signatures of frictional heating and resultant upward surges in the trough region plus to investigate other characteristics of the trough, a set of DMSP line plots is illustrated. As shown in the GPS TEC map of Figure 5, where the DMSP ground track and trough location are also marked, this DMSP pass crossed the trough and thus detected a scenario in the local evening sector over the western region of North America. In this scenario, the T_e line plot tracked increased temperatures (~4500 K), caused by frictional heating and are known as subauroral T_e peak [*Prölss*, 2006], that marked the trough minimum.

At trough latitudes, the V_Z line plot detected increased upward drifts (~250 m/s) that are the signatures of strong upward surges caused by frictional heating. Meanwhile, the V_Y line plot shows the signature of SAPS **E** field [*Foster and Burke*, 2002] appearing as enhanced sunward plasma drifts. Meanwhile, V_Y reaching ~1000 m/s indicates that the SAPS **E** field was quite strong. In this evening scenario, F15 pass-3 tracked (see Ni line plot) the trough with a SED feature (see also 21–24 TECU; indicated in light blue) on its equatorward side and with some large auroral ionization (see also 14–17 TECU; indicated in light green) on its poleward side. Both equatorward and poleward auroral boundaries could be located by utilizing the V_Y line plot [*Horvath and Lovell*, 2009]. We note here that V_Z varied in the auroral zone and some strong ($V_Z \approx 750$ m/s) upward surges occurred there in isolation. Since upward surges were not typical to the auroral zone but were detected as characteristic features of the trough region, the decreased $\Delta(O/N_2)$ in the above described polar map mainly marked trough latitudes.

3.5. Auroral Zone Over North America During the Main Phase

Figure 6 depicts the various characteristics of the auroral zone developed over a larger region of the North American sector during the main phase. Illustrations include a GUVI auroral electron energy flux polar map, a GPS TEC map constructed with data in Figure 2d, a polar $\Delta(O/N_2)$ plot constructed for 0712 UT, and some line plots constructed with King Salmon f_oF_2 and multi-instrument DMSP data. To describe them, the GUVI polar map depicts at 0653 UT a brightened auroral image (100 erg/s/cm^2; indicated in red) in the local afternoon (1400–1800 LT) and evening/nighttime (1800–2400 LT) sectors at ~52°N (geomagnetic). During 0722–0742 UT, GPS TEC (see Figure 6b) tracked some increased auroral ionization caused by particle precipitation (11–21 and 8–11 TECU; indicated in light greens and yellow, respectively) forming a positive phase over North America close to 50°N (geomagnetic; indicated in blue). Equatorward neutral winds, which had been quite strong and exceeded ~1000 m/s according to the CTIP simulated wind vector maps (see one example in Figure 3e), contributed to the maintenance of this positive phase via mechanical wind effects keeping the ionization at higher altitudes of lower recombination. Meanwhile, the ionization remained at a minimum level (5–8 and 2–5 TECU; indicated in orange and dark brown, respectively) elsewhere over the continent forming a negative phase. As this GPS TEC map illustrates, the auroral oval appeared also over the King Salmon ionosonde station. Consequently, as seen in the f_oF_2 data, the storm time data (indicated in dark blue) detected up to 35% auroral-related increases with respect to the quiet time conditions (indicated in blue) but only during 0400–0600 UT due to a data gap. As DMSP F13 passed over west of Alaska, we could investigate the plasma environment of the auroral oval and surrounding ionospheric features. While the subauroral T_e peak (~5000 K) indicates some strong frictional heating, it also marked the trough minimum appearing between a large SED feature and some smaller auroral and polar ionization. Meanwhile, the V_Y and V_Z line plots tracked a strong SAPS **E** field signature ($V_Y = 2572$ m/s) and strong upward surges ($V_Z = 1900$ m/s) at trough latitudes. We note here that some high upward drifts ($V_Z = 1726$ m/s) occurred in the narrow auroral zone that were detected by the F13 spacecraft. These auroral-related upward drifts are close to the trough related upward drifts and thus indicate the strong upwelling of molecular-rich air both in the trough region and in the auroral zone. In good agreement with these DMSP observational results, the polar $\Delta(O/N_2)$ plot shows that the strongest negative thermospheric composition differences (ranging from -0.09 to -0.12; indicated in yellow, orange, and dark brown, respectively) occurred in a wider latitude region, covering both trough and auroral latitudes, in the 150–360°E sector where the auroral oval (i.e., positive phase) developed with the trough (i.e., negative phase). Thus, these negative $\Delta(O/N_2)$ differences were commonly associated with negative and positive storm phases.

3.6. Ionospheric Features Mapped With Two-Cell Polar Convection

Figures 7 and 8 illustrate the distribution of ionospheric plasma under the influence of SAPS **E** field and polar two-cell convection. We have generated some polar convection plots via Virginia Tech's interactive mapping technique (see Figures 7a, 7c, 8a, and 8c) and plotted the previously shown GPS TEC maps in Figures 2c and 2d as polar maps for the Northern Hemisphere (see Figures 7b and 8b). For the Southern Hemisphere, where the GPS TEC data coverage is sparse due to the less number of ground-based receivers, utilizing GIM TEC data that provide continuous coverage was a better option. In order to obtain more meaningful illustrations, we have utilized ΔGIM TEC values, computed as GIM $TEC_{(storm\ time)} - $ GIM $TEC_{(quiet\ time)}$, for constructing the southern polar plots (see Figures 7d and 8d). All these northern and southern polar maps demonstrate that the movements of large-scale ionospheric features were controlled by both the SAPS **E** field and the polar

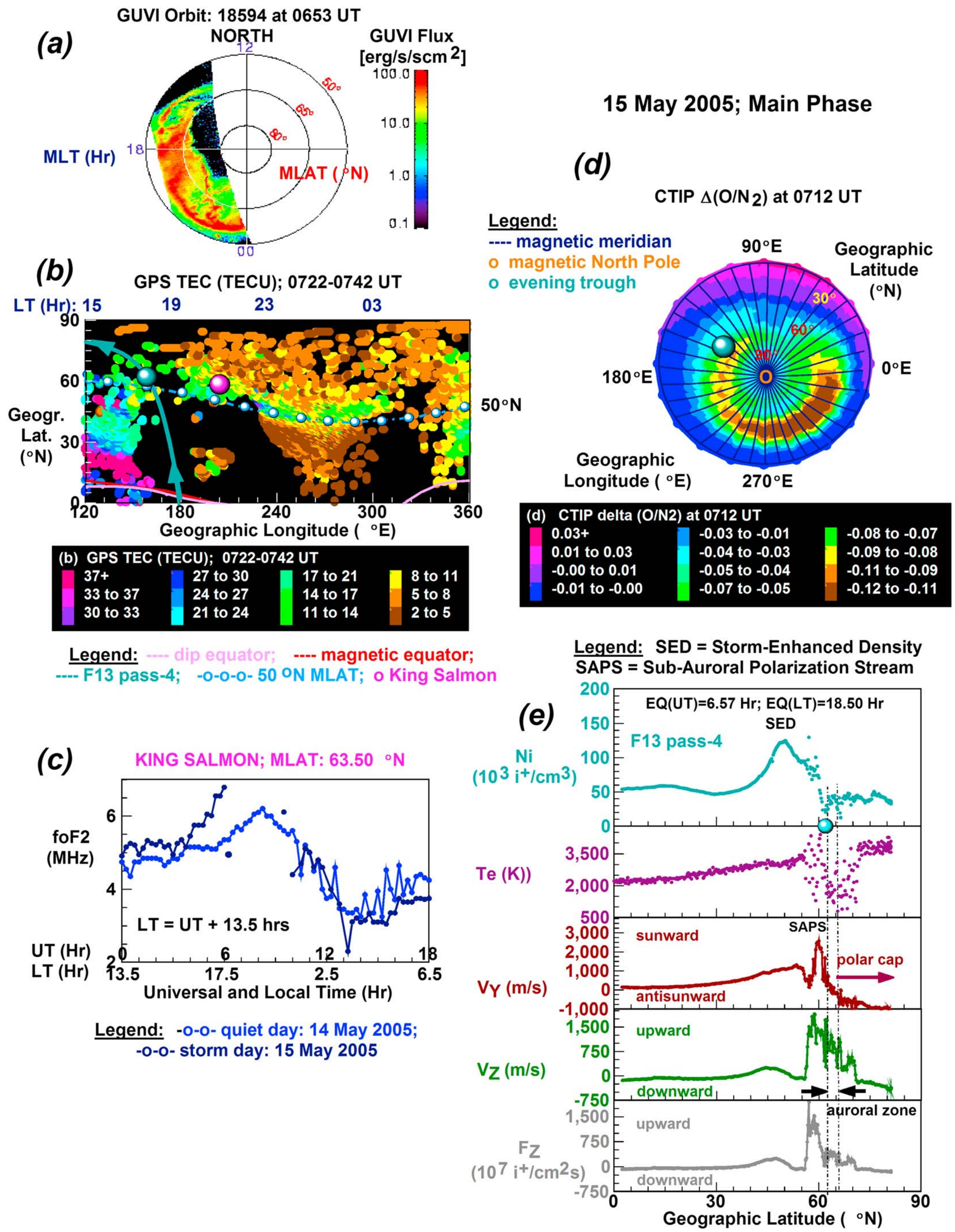

Figure 6. The (a) GUVI auroral electron energy flux polar map and the (b) GPS TEC map show the auroral zone. (c) From King Salmon, the f_oF_2 line plot detected some auroral-related increases. (d) The CTIP $\Delta(O/N_2)$ polar plot illustrates that both the auroral zone and the midlatitude trough related thermospheric composition changes appear as negative values. (e) A multi-instrument DMSP line plot set depicts the SED and the trough with their underlying thermal characteristics and plasma drifts in the local evening sector.

plasma convection. During the initial phase and in the north (see Figure 7b), the SED plume plasma (27–30 TECU; indicated in dark blue) propagated under the influence of SAPS **E** field sunward and thus toward the dayside cusp region (~90°E; 1300 LT) but did not reach it. This left the TEC low (11–14 and 8–11 TECU; indicated in light green and yellow, respectively) in the polar cap region. Furthermore, the TEC reached a minimum (2–6 TECU; indicated in dark brown) in a small region of the magnetic North Pole where

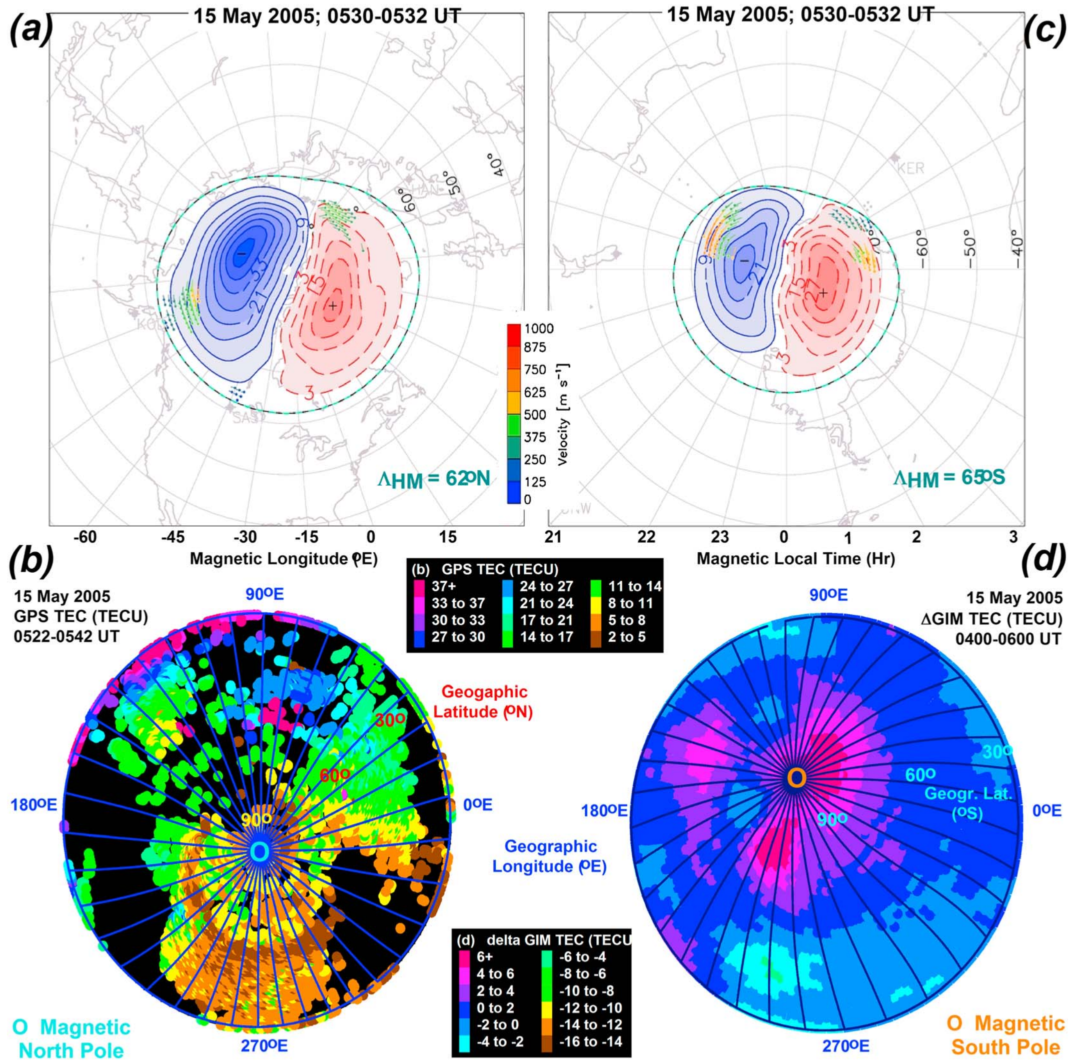

Figure 7. Two scenarios are illustrated for the initial phase. The large-scale convection maps are generated for the (a) northern and (c) southern polar regions. These illustrate that the two-cell convection pattern had been operational at the end of the initial phase. We note here that the interactive plotting tool employed provides color scale for the velocity vectors only and no color scale is provided for the potential pattern mapped. During these scenarios, the polar (b) TEC and (d) ΔTEC plots depict the midlatitude trough with some low and minimum TECs in the northern polar region and a large polar TOI crossing over the magnetic South Pole, respectively.

the solar radiation locally decreased (see P_{solar} plot in Figure 3a). In the south (see Figure 7d), a large TEC enhancement (>6 and 4–6 TECU; indicated in red and pink, respectively) was also driven by the SAPS **E** field and polar convection into the polar region through the dayside cusp (~90°E; 1300 LT). But oppositely to the northern scenario, this large TEC enhancement progressed across the magnetic South Pole, continued on the nightside of the polar cap and thus formed a distinct polar tongue of ionization (TOI) along the antisunward flow channel. Possibly, the higher TECs of this polar TOI were also due to the locally high solar radiation as the southern polar region was sunlit at that time and received almost maximum solar heating (see P_{solar} plot in Figure 3c). During the main phase and in the north (see Figure 8b), some TEC enhancements (14–17 TECU; indicated in light green) entered the polar region through the dayside cusp (30°E; 0900 LT) but did not reach the magnetic pole. Thus, there was no TOI feature present and the northern polar region remained largely a low TEC region (5–8 TECU; indicated in orange) during the local nighttime hours. An opposite scenario occurred on the dayside in the sunlit southern polar region (see Figure 8d). As the SAPS **E** field and sunward polar convection drove some large TEC enhancements (>6 TECU; indicated in red) from the dayside bulge, the enhanced TEC propagated through the dayside cusp (90°E; 1300 LT) into the polar region, reached the

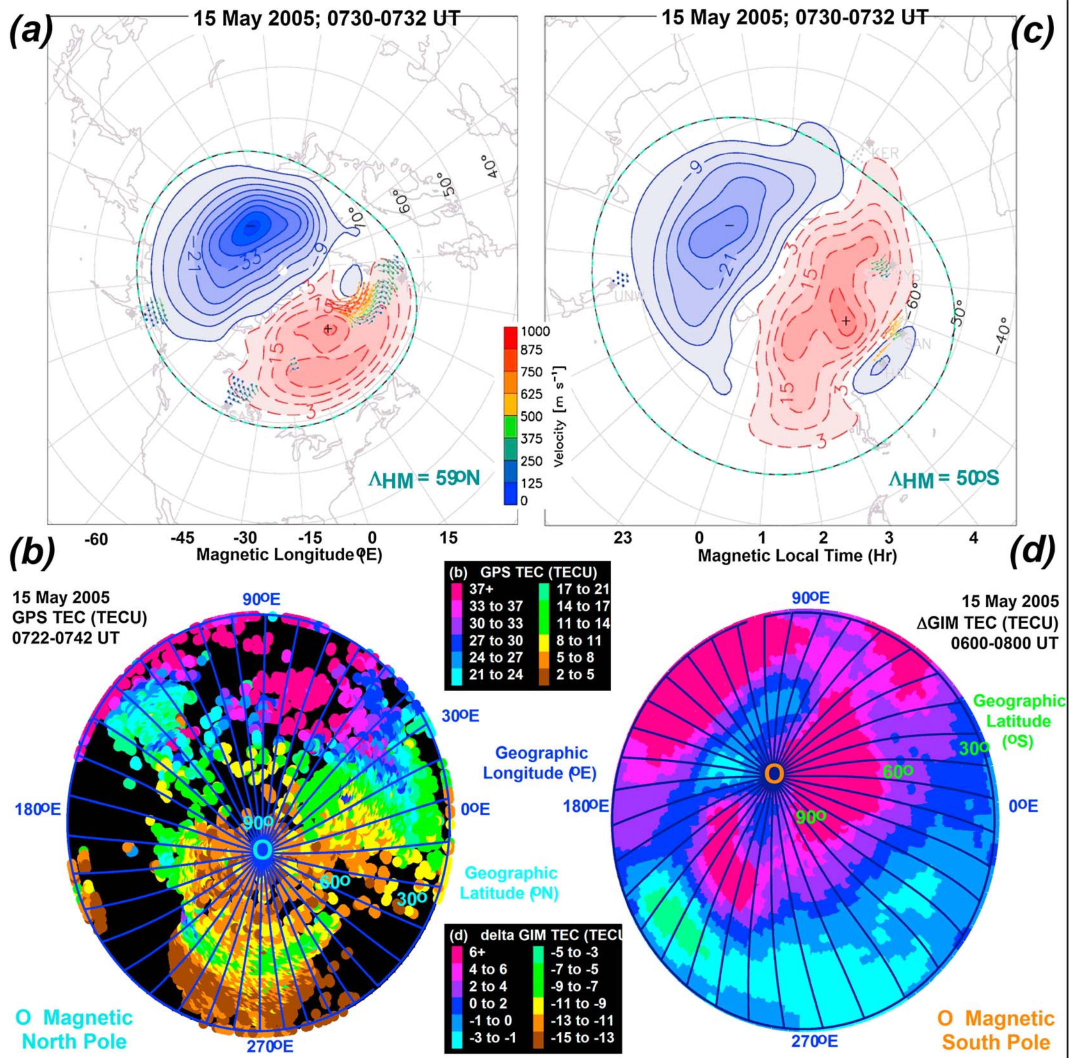

Figure 8. Two scenarios illustrate with large-scale convection maps, generated for the (a) northern and (c) southern polar regions that the two-cell convection pattern had been operational during the first half of the main phase. We note again that the interactive plotting tool employed provides color scale for the velocity vectors only and no color scale is provided for the potential pattern mapped. During these scenarios, the polar (b) TEC and (d) ΔTEC plots depict the auroral zone plus some minimum TECs in the northern polar region and a large polar TOI crossing over the magnetic South Pole, respectively.

magnetic South Pole, and progressed along the antisunward flow channel to the nightside by following the dawn (marked as cross) cell of the convection pattern.

4. Discussions

Our correlations reveal that the polar cap substorm related perturbation **E** field of the initial phase and the undershielding PPEF of the main phase triggered the development of sunward or westward progressing SED plume plasma in the Asian region, close to the POL2 GPS station employed by *Galav et al*. [2014] in their study, causing locally some positive storms there (see Figures 4a and 4b). Meanwhile, the midlatitude trough appeared across the North American continent and also over the ALGO GPS station, utilized by *Galav et al*. [2014], creating a strong negative storm in the narrow (~5 latitude degree) trough region. Consequently, our correlation and observational results add to the study of *Galav et al*. [2014] by providing further observations and verifying their interpretations. Our global GPS TEC map (see Figure 2c) serve as evidence and thus verify that (1) the GPS TEC increase seen in the POL2 GPS data was due to the SED plume plasma and the northern EIA crest occurred at lower latitudes and (2) the midlatitude trough was seen in the ALGO GPS data (e.g., the trough detected by PRN 11 at ~0600 UT in the study of *Galav et al.* [2014] correlates well with this study's map in Figure 2c). However, our global GPS TEC map (see Figure 2c) reveal also that the GPS POL2 and ALGO observations of *Galav et al.* [2014] depict individual and local daytime and nighttime ionospheric features that are not representative of other regions in the daytime and nighttime sectors, respectively.

The coexistence of positive and negative storms is an interesting phenomenon that was first reported by *Lu et al.* [2001] and was observed in this study over North America during the second half of the main phase. Then, a strong auroral oval appearing over North America plus some still existing SED features in the Alaskan region formed together a distinct band of positive phase while the rest of the American longitude sector experienced strong negative storms (see map in Figure 2d). *Lu et al.* [2001] reported such phenomenon occurring under northern winter conditions during the 10 January 1997 geomagnetic storm. They obtained similar observations by utilizing various data but the TEC changes with respect to the quiet time background conditions were derived from TIE-GCM simulated TEC values. This study utilizes GPS TEC maps that are also coupled with a matching GUVI image and some ΔH time series. Since we present actual observations of the auroral oval with GPS TEC maps and GUVI image and we highlight the important role of equatorial downward $\mathbf{E} \times \mathbf{B}$ drift in depleting the equatorial region, our results add to the findings of *Lu et al.* [2001]. We have also included some matching $\Delta(O/N_2)$ polar maps (see Figures 5d and 6d), constructed with CTIP simulated O/N_2 data, that tracked maximum $\Delta(O/N_2)$ decreases at subauroral and auroral latitudes. These polar maps coupled with the DMSP Te, V_Y, and V_Z line plots provide evidence that both the Joule heating in the auroral region and the frictional heating in the subauroral trough region drove upward surges of molecular-rich air from lower altitudes and thus caused significant thermospheric composition changes by significantly decreasing $\Delta(O/N_2)$. It is evident from these observations that O/N_2 decreases can be correlated with both positive (i.e., in the auroral zone) and negative (i.e., in the trough region) storm phases. Our findings are in good agreement with and add to some previous relevant studies utilizing TIE-GCM simulations. *Lu et al.* [2001] utilized the inverse of O/N_2 (i.e., N_2/O) and presented N_2/O increases (equivalent with O/N_2 decreases) confined to the auroral region and *Wang et al.* [2012] documented intense $\Delta(O/N_2)$ depletions in the SAPS (or trough) region.

Finally, we discuss some interesting features seen in the high-latitude plasma density distribution during the main phase/recovery phase transition period (see Figures 7b, 7d, 8b, and 8d). These are the polar TOI in the south creating a positive phase over a larger region of the magnetic South Pole at daytime (see Figures 7d and 8d) and some local minimum plasma densities forming a negative phase over the magnetic North Pole at nighttime (see Figures 7b and 8b). Recently, *Sojka et al.* [2012] demonstrated with modeling results the significance of both solar radiation and high-latitude convection $\mathbf{E}$ field in determining the level of ionization in the polar region, and the favorable conditions created during the local daytime hours that support the development of positive storms in the northern polar region. Showing good consistencies with the results of *Sojka et al.* [2012], this study reports similar findings for the daytime southern polar region and an opposite scenario for the nighttime northern polar region where some negative storms developed. For the time periods covered by the polar TEC plots and convection maps (see Figures 7a, 7c, 8a, and 8c), we have also studied CTIPe simulated solar heating (P_{solar}) and Joule heating (P_{Joule}) values (see Figures 3a and 3c). While the Joule heating was uniformly close to zero over both magnetic poles, the solar heating showed a direct correlation with the level of TEC in the polar region (see Figures 7b, 7d, 8b, and 8d). Minimum nighttime TECs created a negative phase when solar heating reached a local minimum over the magnetic North Pole, while maximum daytime TECs formed a positive phase when solar heating locally maximized over the magnetic South Pole. Furthermore, by comparing the two southern daytime scenarios, the enlargement of polar TEC enhancements during the course of the geomagnetic storm is evident. This is due to the expansion of polar cap region (from 65 to 50°S, invariant; and indicated as Λ_{HB} in Figures 7d and 8d, respectively) implying both the strengthening of convection $\mathbf{E}$ field that in turn increased the polar convection and the increase of so-called snow-plow effect [*Foster*, 1993] transporting more plasma from midlatitudes. Consequently, the strengthening of convection $\mathbf{E}$ field played also a crucial factor, additionally to the locally maximizing solar heating, for the better development of positive storms in the daytime southern polar region. Meanwhile, the lesser expansion of northern polar cap region (from 62 to 59°N, invariant; and indicated as Λ_{HB} in Figures 7b and 8b, respectively) implies a smaller increase both in convection $\mathbf{E}$ field and in polar convection and therefore weaker snow-plow effects. During this time, the TEC had become quite depleted in the nighttime polar region. Thus, a weaker convection **E** field plus the locally minimized solar heating were mainly responsible for creating negative storms in the nighttime northern polar region.

5. Conclusions

We have utilized a variety of observational results and model simulations for identifying the plasma density features that formed positive and negative storm phases and their spatial variations during the 15 May 2005 geomagnetic superstorm. Since the initial phase started at ~0300 UT, the local daytime (nighttime) sector covered the 0–180°E (180–360°E) hemisphere. Our global observations and CTIPe model simulations provide evidence that during the initial and main geomagnetic storm phases the sunward progressing SED plume plasma characterized by a maximum $\Delta(O/N_2)$ of 0.02 formed positive ionospheric storm at midlatitudes over Asia and the midlatitude trough characterized by a minimum $\Delta(O/N_2)$ of -0.07 created negative ionospheric storm over North America. Thus, each ionospheric storm manifested itself as an individual ionospheric feature with a distinctive composition change. Since these resultant ionospheric features appeared locally, we conclude that they were not representative of the entire midlatitude region of their respective hemispheres. However, as our results reveal, there was a significant longitude-dependent variation due to the main phase-related undershielding PPEF. Then, some positive (negative) ionospheric storms dominated the 50°N–45°S geomagnetic latitude region of the dayside (nightside) hemisphere. We have also analyzed the development of negative ionospheric storms at polar, middle, and low latitudes and conclude that their corresponding causative mechanisms are (1) the local solar radiation decrease in the northern polar region, (2) a well-developed midlatitude trough, and (3) a strong equatorial $\mathbf{E}\times\mathbf{B}$ downward drift driven by the westward undershielding PPEF, respectively. Our GPS TEC and GUVI observations also demonstrate the interesting phenomenon of simultaneously occurring positive and negative ionospheric storms over North America. Finally, we conclude that for the first time, this study's polar observations demonstrate and provide evidence that the more (less) intensive strengthening of polar convection **E** field and the locally maximizing (minimizing) solar heating at daytime (nighttime) over the magnetic South (North) Pole played crucial roles in producing positive (negative) ionospheric storms in the southern (northern) polar cap region.

Acknowledgments
This material is based on research sponsored by the Air Force Research Laboratory, under agreement FA2386-14-1-4077. The U.S. Government is authorized to reproduce and distribute reprints for Governmental purposes notwithstanding any copyright notation thereon. We are grateful to the ACE SWEPAM instrument team and the ACE Science Center for providing the ACE data. We gratefully acknowledge the Center for Space Sciences at the University of Texas at Dallas and the U.S. Air Force for providing the DMSP thermal plasma data. We also thank the World Data Center for Geomagnetism at Kyoto (http://wdc.kugi.kyoto-u.ac.jp/wdc/Sec3.html) for providing the geomagnetic data and indices and the Space Physics Interactive Data Resource (SPIDR) for the magnetic data (http://spidr.ngdc.noaa.gov/spidr/dataset.do?view=geomagnetic). Special thanks are extended to JPL for the GIM data, to the Madrigal Database at Haystack Observatory (http://madrigal.haystack.mit.edu/madrigal) for providing the ground-based GPS TEC data, and to the NASA MO&DA program for the GUVI image (http://guvi.jhuapl.edu/site/guvi-index.shtml). We are thankful to Virginia Polytechnic Institute and State University for the Interactive Map Potential Plotting tool (http://vt.superdarn.org/tiki-index.php?page=DaViT+Map+Potential+Plot) and to the Community Coordinated Modeling Center at NASA Goddard Space Flight Center for the CTIP and CTIPe model simulations. Simulation results have been provided by the Community Coordinated Modeling Center through their public Runs on Request system (http://ccmc.gsfc.nasa.gov). The CCMC is a multiagency partnership between NASA, AFMC, AFOSR, AFRL, AFWA, NOAA, NSF, and ONR. The CTIPe model was developed by T. Fuller-Rowell at the Space Environment Center (NOAA SEC).

M. Balikhin thanks two anonymous reviewers for their assistance in evaluating this paper.

References

Abdu, M. A. (1997), Major phenomena of the equatorial ionosphere thermosphere system under disturbed conditions, *J. Atmos. Sol. Terr. Phys.*, *59*, 1505–1519.

Anderson, D., K. Yumoto, M. Ishitsuka, and E. Kudeki (2002), Estimating daytime vertical ExB drift velocities in the equatorial F-region using ground-based magnetometer observations, *Geophys. Res. Lett.*, *29*(12), 1596, doi:10.1029/2001GL0144562.

Balan, N., and G. J. Bailey (1995), Equatorial plasma fountain and its effects: Possibility of an additional layer, *J. Geophys. Res.*, *100*(A11), 21,421–21,432, doi:10.1029/95JA01555.

Balan, N., K. Shiokawa, Y. Otsuka, T. Kikuchi, D. Vijaya Lekshmi, S. Kawamura, M. Yamamoto, and G. J. Bailey (2010), A physical mechanism of positive ionospheric storms at low and mid latitudes, *J. Geophys. Res.*, *115*, A02304, doi:10.1029/2009JA014515.

Balan, N., Y. Otsuka, M. Nishioka, J. Y. Liu, and G. J. Bailey (2013), Physical mechanisms of the ionospheric storms at equatorial and higher latitudes during the recovery phase of geomagnetic storms, *J. Geophys. Res. Space Physics*, *118*, 2660–2669, doi:10.1002/jgra.50275.

Basu, S., S. Basu, E. MacKenzie, C. Bridgwood, C. E. Valladares, K. M. Groves, and C. Carrano (2010), Specification of the occurrence of equatorial ionospheric scintillations during the main phase of large magnetic storms within solar cycle 23, *Radio Sci.*, *45*, RS5009, doi:10.1029/2009RS004343.

Bisi, M. M., et al. (2010), From the Sun to the Earth: The 13 May 2005 coronal mass ejection, *Sol. Phys.*, *265*(1), 49–127, doi:10.1007/s11207-010-9602-8.

Blanc, M., and A. D. Richmond (1980), The ionospheric disturbance dynamo, *J. Geophys. Res.*, *85*(A4), 1669–1699, doi:10.1029/JA085iA04p01669.

Cander, L. R., and S. J. Mihajlovic (2005), Ionospheric spatial and temporal variations during the 29–31 October 2003 storm, *J. Atmos. Sol. Terr. Phys.*, *67*, 1118–1128, doi:10.1016/j.jastp.2005.02.020.

Christensen, A. B., et al. (2003), Initial observations with the Global Ultraviolet Imager (GUVI) in the NASA TIMED satellite mission, *J. Geophys. Res.*, *108*(A12), 1451, doi:10.1029/2003JA009918.

Danilov, A. D., and L. D. Morozova (1985), Ionospheric storms in the F2 region: Morphology and physics (Review), *Geomagn. Aeron.*, *25*, 593–605.

Dashora, N., S. Sharma, R. S. Dabas, S. Alex, and R. Pandey (2009), Large enhancements in low latitude total electron content during 15 May 2005 geomagnetic storm in Indian zone, *Ann. Geophys.*, *27*, 1803–1820, doi:10.5194/angeo-27-1803-2009.

Fejer, B. G., J. W. Jensen, T. Kikuchi, M. A. Abdu, and J. L. Chau (2007), Equatorial ionospheric electric fields during the November 2004 magnetic storm, *J. Geophys. Res.*, *112*, A10304, doi:10.1029/2007JA012376.

Foster, J. C. (1993), Storm time plasma transport at middle and high latitudes, *J. Geophys. Res.*, *98*(A2), 1675–1689, doi:10.1029/92JA02032.

Foster, J. C., and W. J. Burke (2002), SAPS: A new characterization for sub-auroral electric fields, *EoS Trans. AGU*, *83*, 393, doi:10.1029/2002EO000289.

Foster, J. C., et al. (2005), Multiradar observations of the polar tongue of ionization, *J. Geophys. Res.*, *110*, A09S31, doi:10.1029/2004JA010928.

Fuller-Rowell, T. J., G. H. Millward, A. D. Richmond, and M. V. Codrescu (2002), Storm-time changes in the upper atmosphere at low latitudes, *J. Atmos. Sol. Terr. Phys.*, *64*(12–14), 1383–1391, doi:10.1016/S1364-6826(02)00101-3.

Galav, P., S. S. Rao, S. Sharma, G. Gordiyenko, and R. Pandey (2014), Ionospheric response to the geomagnetic storm of 15 May 2005 over midlatitudes in the day and night sectors simultaneously, *J. Geophys. Res. Space Physics*, *119*, 5020–5031, doi:10.1002/2013JA019679.
Horvath, I. (2007), Impact of 10 January 1997 geomagnetic storm on the nighttime Weddell Sea Anomaly: A study utilizing data provided by the TOPEX/Poseidon mission and the Defense Meteorological Satellite Program, and simulations generated by the Coupled Thermosphere/Ionosphere Plasmasphere model, *J. Geophys. Res.*, *112*, AO6329, doi:10.1029/2006JA012153.
Horvath, I., and B. C. Lovell (2009), Distinctive plasma density features of the topside ionosphere and their electrodynamics investigated during southern winter, *J. Geophys. Res.*, *114*, A01304, doi:10.1029/2008JA013683.
Kelley, M. C., M. N. Vlasov, J. C. Foster, and A. J. Coster (2004), A quantitative explanation for the phenomenon known as storm-enhanced density, *Geophys. Res. Lett.*, *31*, L19809, doi:10.1029/2004GL020875.
Kikuchi, T., T. Araki, H. Maeda, and K. Maekawa (1978), Transmission of polar electric fields to the equator, *Nature*, *273*, 650–651, doi:10.1038/273650a0.
Kikuchi, T., K. K. Hashimoto, and K. Nozaki (2008), Penetration of magnetospheric electric fields to the equator during a geomagnetic storm, *J. Geophys. Res.*, *113*, A06214, doi:10.1029/2007JA012628.
Kintner, P. M., B. M. Ledvina, and E. R. de Paula (2007), GPS and ionospheric scintillations, *Space Weather*, *5*, S09003, doi:10.1029/2006SW000260.
Kozyreva, O. V., and N. G. Kleimenova (2007), Geomagnetic pulsations and magnetic disturbances during the initial phase of a strong magnetic storm of May 15, 2005, *Geomagn. Aeron.*, *47*(4), 501–511, doi:10.1134/S001679320704007X.
Vijaya Lekshmi, D., N. Balan, V. K. Vaidyan, H. Alleyne, and G. J. Bailey (2007), Response of the ionosphere to super geomagnetic storms: Observations and modeling, *Adv. Space Res.*, *41*, 548–555, doi:10.1016/j.asr.2007.08.029.
Lu, G., A. D. Richmond, R. G. Roble, and B. A. Emery (2001), Coexistence of ionospheric positive and negative storm phases under northern winter conditions: A case study, *J. Geophys. Res.*, *106*(A11), 24,493–24,504, doi:10.1029/2001JA000003.
Lu, G., L. P. Goncharenko, M. J. Nicolls, A. I. Maute, A. J. Coster, and L. J. Paxton (2012), Ionospheric and thermospheric variations associated with prompt penetration electric fields, *J. Geophys. Res.*, *117*, A08312, doi:10.1029/2012JA017769.
Mannucci, A. J., B. T. Tsurutani, B. A. Iijima, A. Komjathy, A. Saito, W. D. Gonzalez, F. L. Guarnieri, J. U. Kozyra, and A. Skoug (2005), Dayside global ionospheric response to the major interplanetary events of October 29–30, 2003 "Halloween Storms", *Geophys. Res. Lett.*, *32*, L12S02, doi:10.1029/2004GL021467.
Mendillo, M. (2006), Storms in the ionosphere: Patterns and processes for total electron content, *Rev. Geophys.*, *44*, RG4001, doi:10.1029/2005RG000193.
Millward, G. H., R. J. Moffett, S. Quegan, and T. J. Fuller-Rowell (1993), Effects of an atmospheric gravity wave on the midlatitude ionospheric *F* layer, *J. Geophys. Res.*, *98*(A11), 19,173–19,179, doi:10.1029/93JA02093.
Prölss, G. W. (2006), Subauroral electron temperature enhancement in the nighttime ionosphere, *Ann. Geophys.*, *24*(7), 1871–1885, doi:10.5194/angeo-24-1871-2006.
Prölss, G. W., and M. J. Jung (1978), Traveling atmospheric disturbances as a possible explanation for daytime positive storm effects of moderate duration at middle latitudes, *J. Atmos. Sol. Terr. Phys.*, *40*, 1351–1354, doi:10.1016/0021-9169(78)90088-0.
Roble, R. G., R. E. Dickinson, and E. C. Ridley (1982), Global circulation and temperature structure of thermosphere with high-latitude plasma convection, *J. Geophys. Res.*, *87*(A3), 1599–1614, doi:10.1029/JA087iA03p01599.
Sahai, Y., et al. (2009), Effects observed in the Latin American sector ionospheric F region during the intense geomagnetic disturbances in the early part of November 2004, *J. Geophys. Res.*, *114*, A00A19, doi:10.1029/2007JA013007.
Sastri, J. H., N. Jyoti, V. V. Somayajulu, H. Chandra, and C. V. Devasia (2000), Ionospheric storm of early November 1993 in the Indian equatorial region, *J. Geophys. Res.*, *105*(A8), 18,443–18,455, doi:10.1029/1999JA000372.
Scharroo, R., and W. H. F. Smith (2010), A global positioning system–based climatology for the total electron content in the ionosphere, *J. Geophys. Res.*, *115*, A10318, doi:10.1029/2009JA014719.
Schunk, R. W., and J. J. Sojka (1996), Ionosphere-thermosphere space weather issues, *J. Atmos. Sol. Terr. Phys.*, *58*, 1527–1574, doi:10.1016/0021-9169(96)00029-3.
Sharma, S., P. Galav, N. Dashora, and R. Pandey (2011), Longitudinal study of the ionospheric response to the geomagnetic storm of 15 May 2005 and manifestation of TADs, *Ann. Geophys.*, *29*, 1063–1070, doi:10.5194/angeo-29-1063-2011.
Sojka, J. J., M. David, R. W. Schunk, and R. A. Heelis (2012), A modeling study of the longitudinal dependence of storm time midlatitude dayside total electron content enhancements, *J. Geophys. Res.*, *117*, A02315, doi:10.1029/2011JA017000.
Su, Y.-J., M. F. Thomsen, J. E. Borovsky, and J. C. Foster (2001), A linkage between polar patches and plasmaspheric drainage plumes, *Geophys. Res. Lett.*, *28*(1), 111–113, doi:10.1029/2000GL012042.
Troshichev, O., H. Hayakawa, A. Matsuoka, T. Mukai, and K. Tsuruda (1996), Cross polar cap diameter and voltage as a function of PC index and interplanetary quantities, *J. Geophys. Res.*, *101*(A6), 13,429–13,435, doi:10.1029/95JA03672.
Tsurutani, B., et al. (2004), Global dayside ionospheric uplift and enhancement associated with interplanetary electric fields, *J. Geophys. Res.*, *109*, A08302, doi:10.1029/2003JA010342.
van der Meeren, C., K. Oksavik, D. Lorentzen, J. I. Moen, and V. Romano (2014), GPS scintillation and irregularities at the front of an ionization tongue in the nightside polar ionosphere, *J. Geophys. Res. Space Physics*, *119*, 8624–8636, doi:10.1002/2014JA020114.
Wang, W., J. Lei, A. G. Burns, S. C. Solomon, M. Wiltberger, J. Xu, Y. Zhang, L. Paxton, and A. Coster (2010), Ionospheric response to the initial phase of geomagnetic storms: Common features, *J. Geophys. Res.*, *115*, A07321, doi:10.1029/2009JA014461.
Wang, W., E. R. Talaat, A. G. Burns, B. Emery, S. Hsieh, J. Lei, and J. Xu (2012), Thermosphere and ionosphere response to subauroral polarization streams (SAPS): Model simulations, *J. Geophys. Res.*, *117*, A07301, doi:10.1029/2012JA017656.